Filter-matrix lattice Boltzmann model for microchannel gas flows

Congshan Zhuo* and Chengwen Zhong†

National Key Laboratory of Science and Technology on Aerodynamic Design and Research, Northwestern Polytechnical University, Xi'an, Shaanxi 710072, China

(Received 30 July 2013; published 25 November 2013)

The lattice Boltzmann method has been shown to be successful for microscale gas flows, and it has attracted significant research interest. In this paper, the recently proposed filter-matrix lattice Boltzmann (FMLB) model is first applied to study the microchannel gas flows, in which a Bosanquet-type effective viscosity is used to capture the flow behaviors in the transition regime. A kinetic boundary condition, the combined bounce-back and specular-reflection scheme with the second-order slip scheme, is also designed for the FMLB model. By analyzing a unidirectional flow, the slip velocity and the discrete effects related to the boundary condition are derived within the FMLB model, and a revised scheme is presented to overcome such effects, which have also been validated through numerical simulations. To gain an accurate simulation in a wide range of Knudsen numbers, covering the slip and the entire transition flow regimes, a set of slip coefficients with an introduced fitting function is adopted in the revised second-order slip boundary condition. The periodic and pressure-driven microchannel flows have been investigated by the present model in this study. The numerical results, including the velocity profile and the mass flow rate, as well as the nonlinear pressure distribution along the channel, agree fairly well with the solutions of the linearized Boltzmann equation, the direct simulation Monte Carlo results, the experimental data, and the previous results of the multiple effective relaxation lattice Boltzmann model. Also, the present results of the velocity profile and the mass flow rate show that the present model with the fitting function can yield improved predictions for the microchannel gas flow with higher Knudsen numbers in the transition flow regime.

DOI: 10.1103/PhysRevE.88.053311 PACS number(s): 47.11.−j

I. INTRODUCTION

Due to technological advances in microelectromechanical systems (MEMSs) and their growing application areas, microscale gas flows (microfluidics) have attracted an increasing amount of attention in the past few decades [1–3]. Microscale gas flows behave differently from that predicted by macroscopic theory, and they are usually characterized by a dimensionless parameter, namely the Knudsen number $\mathrm{Kn} = \lambda/H$, where λ is the mean free path of gas molecules and H is a characteristic length of the flow system. MEMS devices involving gas flows typically operate in the slip flow regime ($0.001 < \mathrm{Kn} \leqslant 0.1$) and the transition flow regime ($0.1 < \mathrm{Kn} \leqslant 10$) [4] due to their small length scales, which become comparable with the molecular mean free path. It is well accepted that the conventional Navier-Stokes (NS) equations based on the continuum assumption are normally valid in the continuum flow regime ($\mathrm{Kn} \leqslant 0.001$), and they can also be extended as far as $\mathrm{Kn} \leqslant 0.1$ with the introduction of slip boundary conditions. Once $\mathrm{Kn} > 0.1$, the continuum and thermodynamic equilibrium assumptions begin to break down and the rarefaction effects dominate the flow characteristics [5]. To model gas flows ranging from the continuum regime to the free molecular regime ($\mathrm{Kn} > 10$) and to capture the rarefaction effects exactly, it is necessary to solve the Boltzmann equation. However, this proves to be difficult and even impractical except in a few cases, because the intermolecular collisions are quite important when $\mathrm{Kn} < 10$ and the collision integral term in the Boltzmann equation is very expensive to solve. In the past two decades, the direct simulation Monte Carlo (DSMC) method [6], based on the gas kinetic theory, has emerged as the dominant numerical technique and has become the most widely used approach for solving gas flows in the transition regime, but it is computationally demanding in practical engineering applications.

On the other hand, some other mesoscopic methods based on the gas kinetic theory have also been proposed and applied to study microscale gas flows, such as the discrete-velocity method (DVM) [7], the gas-kinetic scheme (GKS) [8,9] and the lattice Boltzmann method (LBM) [10,11]. Compared to these numerical methods, the LBM has distinctive computational features, such as easy implementation due to its simple structure, parallelization in nature due to the locality of particle interaction and the transport of particle information, and reliable numerical robustness [12–14]. Actually, the LBM has attracted an increasing amount of attention in recent years, and it is considered to be a promising approach for low-speed microscale gas flows.

Although the LBM has been shown to be successful for microscale gas flows in the past decade [14,15], most of the previous studies of the LBM were focused on devising mesoscopic boundary conditions to precisely predict the slip phenomenon of rarefied gas flow in the slip regime [10,11,16–25]. For microscale gas flows with moderate and high Knudsen numbers, the standard lattice Boltzmann (LB) models with a slip boundary condition are insufficient to capture the kinetic boundary layers, or the Knudsen layers, that appear in the solutions of the Boltzmann equation near solid boundaries [26,27]. The standard LBM captures just a few low-order moments of the solutions of the true Boltzmann equation, that is to say, it is only accurate at the NS level as an approximation to the Boltzmann equation [27,28]. Thus,

*zhuocs@mail.nwpu.edu.cn
†Corresponding author: zhongcw@nwpu.edu.cn

just like the NS equations, the standard LBM is incapable of describing the gas motion within the Knudsen layer, and will fail to work for high-Kn flows where the Knudsen layer take a large portion of flow domain [26]. Recently, Zhang [15] reviewed and discussed the LBM models and their applications for microfluidics.

To improve the capability of the LBM for high-Kn flows in the transition regime, two approaches have been proposed: one is to design a higher-order LBM via increasing the number of discrete velocities, and another is to introduce the effective viscosity method into the LB models. Some higher-order or multispeed LB models have been developed to increase the approximation accuracy to the continuous Boltzmann equation [28–32]. However, Kim *et al*. [33] recently showed that the accuracy of the higher-order LBM did not increase monotonically with the increases of the order of Gauss-Hermite quadrature, and this method could not guarantee an improved accuracy for microscale gas flow with the Knudsen number up to $\mathrm{Kn} = \mathrm{O}(1)$.

On the other hand, as reported in Ref. [26], taking the gas-wall collision effects into account for a confined gas, the local mean free path is affected significantly by the wall boundaries, which are much smaller than that defined in unbounded systems; especially for high-Kn flows, the mean free path becomes comparable with the characteristic length, and the Knudsen layer will take a large portion of flow domain. Therefore, by introducing an effective relaxation time that corresponds to the effective mean free path, the Navier-Stokes-aimed LB models are also capable of capturing the effects of the Knudsen layer for microscale gas flow in the transition regime, as shown in recent studies [26,34–40]. In the literature, two kinds of strategies have been applied for the LB investigations of microscale gas flow. One is using a geometry-dependent expression of local effective viscosity, such as the correction $\mu_e = \mu/(1 + 0.7e^{-C y/\lambda})$ with an empirical parameter C proposed by Zhang *et al*. [34], and the other is that based on the Stops expression $\mu_e = \Phi(y, \mathrm{Kn})\mu$ used by Guo *et al*. [26], Tang *et al*. [36], and Liu and Guo [40]. Note that, as reported by Li *et al*. [37], the Stops-based function $\Phi(y, \mathrm{Kn})$ is complicated, and it contains an exponential integral function $E_i(\gamma) = \int_1^\infty t^{-1} e^{-\gamma t} dt$ ($\gamma \sim y/\lambda$), which requires a numerical integration and thus will reduce the computational efficiency significantly. Although corrections can improve the numerical accuracy to some extent, it still cannot give satisfactory results for microscale gas flows with higher Knudsen numbers.

Another type of effective viscosity is to design a non-geometry-dependent expression which only takes the average effect into consideration, e.g., the Bosanquet-type expression $\mu_e = \mu/(1 + a\,\mathrm{Kn})$ presented in the previous studies on the microchannel gas flows using the traditional numerical methods [41,42] where the viscosity has been averaged over the channel cross section. In other words, the real local viscosity is not considered in the simulations, and the effective viscosity only takes the overall rarefaction effect on gas viscosity into consideration. Recently, Michalis *et al*. [43] investigated the effects of rarefaction on gas viscosity through the DSMC simulations of microchannel gas flow, demonstrating that the Bosanquet-type of approximation describes very satisfactorily the Knudsen number dependence of the viscosity over the entire transition flow regime. By incorporating the Bosanquet-type effective viscosity into the LBM frameworks, Li *et al*. [37] and Homayoon *et al*. [38] successfully simulated microchannel gas flows in the transition regime using the MRT and LBGK models with different slip boundary conditions, respectively. Li *et al*.'s study showed that taking the Bosanquet-type effective viscosity and employing an appropriate slip boundary condition can give satisfactory results for microchannel gas flow at moderate Knudsen numbers (up to $\mathrm{Kn} \approx 3$), but it still cannot provide satisfactory results for the mass flow rate at relatively large Knudsen numbers ($4 < \mathrm{Kn} \leqslant 10$) in the transition regime. The main reason behind the deviation may be that the constant slip coefficients used in the second-order slip boundary condition, in which the effects of effective viscosity are included, are inappropriate for relatively large Kn flow simulations in the transitional regime.

In this study, we present an extended filter-matrix lattice Boltzmann (FMLB) model [44] with Bosanquet-type effective viscosity to study microchannel gas flows in the slip and entire transition regime. Following the literature [22,26], we first analyze a kinetic boundary condition for the FMLB model in detail, and then we present an appropriate slip boundary condition taking into account the discrete effects for the simulations of microchannel gas flow. Finally, inspired by Guo *et al*.'s study [26], we proposed a corrected slip boundary condition, which contains an adjustable coefficient as a function of the local Knudsen number, to improve the capability of the present model in predicting a reasonable mass flow rate for relatively large Knudsen numbers in the transition regime.

The rest of the paper is organized as follows. The extended FMLB model is described in Sec. II. The kinetic boundary condition for the FMLB model is constructed and analyzed in Sec. III. Section IV is used to present and discuss in detail the simulation results of microchannel gas flows in the slip and entire transition regimes. Finally, some concluding remarks drawn from this study are made in Sec. V.

II. THE FMLB MODEL FOR MICROSCALE GAS FLOW

A. The FMLB model

Considering the staggered formulation of the discrete velocity Boltzmann equation (DVBE) for the time-space discretization, the evolution equation of the discrete density distribution function N_i for the gas molecules reads [44–46]

$$N_i\left(\vec{x} + \frac{\vec{c}_i\delta_t}{2}, t + \frac{\delta_t}{2}\right) - N_i\left(\vec{x} - \frac{\vec{c}_i\delta_t}{2}, t - \frac{\delta_t}{2}\right) = \delta_t \Omega_i(N), \tag{1}$$

where $\vec{c}_i$ is the discrete particle velocity in the ith direction, δ_t is the time step, and $\Omega_i\,(N)$ represents the discrete collision operator, which includes the external force term and obeys the basic conservation laws of mass and momentum:

$$\sum_i \Omega_i\,(N) = 0, \quad \sum_i \vec{c}_i\,\Omega_i\,(N) = \vec{f}, \tag{2}$$

where $\vec{f}$ is the body force experienced by the molecules.

For the two-dimensional (2D) applications and without loss of generality, we consider the D2Q9 model in this work, and

the discrete velocity $\vec{c}_i$ is defined as

$$\vec{c}_i = \begin{cases} (0,0)^t, & i = 0, \\ c(\pm 1,0)^t, c(0,\pm 1)^t, & i = 1-4, \\ c(\pm 1,\pm 1)^t, & i = 5-8, \end{cases} \tag{3}$$

where $c = \delta_x/\delta_t$ is the lattice speed, with δ_x being the lattice size.

To guarantee the recovery from Eq. (1) to the continuity and momentum equations in the Navier-Stokes level, by assuming constant kinematic viscosity ($B = \nu_B/\nu = 1$, with B denoting the ratio of the bulk kinematic viscosity to the local kinematic viscosity), the solution for the density distribution function N_i can be expressed as (see [44] for details)

$$\begin{aligned} N_i = \rho\omega_i \Bigg[& 1 + \frac{\vec{c}_i \cdot \vec{u}}{c_s^2} + \frac{1}{2}\left(\frac{(\vec{c}_i \cdot \vec{u})^2}{c_s^4} - \frac{\vec{u} \cdot \vec{u}}{c_s^2} \right) \\ & - \nu \left(\frac{(\vec{c}_i \cdot \vec{\nabla})(\vec{c}_i \cdot \vec{u})}{c_s^4} - \frac{\vec{\nabla} \cdot \vec{u}}{c_s^2} \right) \Bigg], \\ & i = 0,1,\ldots,8, \end{aligned} \tag{4}$$

where for the D2Q9 model, the weight factor, ω_i, takes the values $\omega_0 = 4/9$, $\omega_{1-4} = 1/9$, and $\omega_{5-8} = 1/36$, and $c_s = \sqrt{RT} = c/\sqrt{3}$ is the sound speed, with R being the gas constant and T the system temperature. The macroscopic density and velocity are defined as

$$\rho = \sum_i N_i(\vec{x},t), \quad \rho\vec{u} = \sum_i \vec{c}_i N_i(\vec{x},t). \tag{5}$$

Substituting Eq. (4) into Eq. (1) with some high-order terms dropped, the discrete collision operator $\Omega_i(N)$ can be written as [44]

$$\Omega_i(N) = \frac{\rho\omega_i}{c_s^2}\left[(\vec{c}_i \cdot \vec{\nabla})(\vec{c}_i \cdot \vec{u}) - c_s^2 \vec{\nabla} \cdot \vec{u}\right] + \frac{\omega_i}{c_s^2}\vec{c}_i \cdot \vec{f}. \tag{6}$$

With Eq. (1) taken into consideration, the first-order Taylor expansions of $N_i(\vec{x} \pm \vec{c}_i\delta_t/2, t \pm \delta_t/2)$ lead to

$$N_i\left(\vec{x} \pm \frac{\vec{c}_i\delta_t}{2}, t \pm \frac{\delta_t}{2}\right) = N_i(\vec{x},t) \pm \frac{1}{2}\delta_t \Omega_i(N). \tag{7}$$

Based on the discrete velocity vectors given by Eq. (3), we can define two moment vectors,

$$\alpha_k^{\pm} = \sum_i E_{ki} N_i\left(\vec{x} \pm \frac{\vec{c}_i\delta_t}{2}, t \pm \frac{\delta_t}{2}\right), \tag{8}$$

where the corresponding invertible filter matrix E_{ki} for the D2Q9 model is given by

$$\begin{aligned} E_{ki} = \Big[& 1, c_{ix}, c_{iy}, 3c_{ix}^2 - 1, 3c_{ix}c_{iy}, 3c_{iy}^2 - 1, c_{ix}\left(3c_{iy}^2 - 1\right), \\ & c_{iy}\left(3c_{ix}^2 - 1\right), \left(3c_{ix}^2 - 1\right)\left(3c_{iy}^2 - 1\right)/2 \Big]^{\mathrm{T}}. \end{aligned} \tag{9}$$

Also, the density distribution function $N_i(\vec{x} \pm \vec{c}_i\delta_t/2, t \pm \delta_t/2)$ can be rewritten as a product of the inverse matrix E_{ki}^{-1} and the moment vector $\alpha_k^{\pm}$.

Substituting Eqs. (4), (6), (7), and (9) into Eq. (8), the moment vectors $\alpha_k^{\pm}$ can be written as

$$\alpha_k^{\pm} = \begin{bmatrix} \rho \\ \rho u_x \pm \frac{\delta_t}{2} f_x \\ \rho u_y \pm \frac{\delta_t}{2} f_y \\ 3\rho u_x u_x + \rho(-6\nu \pm \delta_t)\frac{\partial u_x}{\partial x} \\ 3\rho u_x u_y + \frac{\rho(-6\nu \pm \delta_t)}{2}\left(\frac{\partial u_x}{\partial y} + \frac{\partial u_y}{\partial x}\right) \\ 3\rho u_y u_y + \rho(-6\nu \pm \delta_t)\frac{\partial u_y}{\partial y} \\ T_1^{\pm} \\ T_2^{\pm} \\ F^{\pm} \end{bmatrix}, \tag{10}$$

where $T_{1,2}^{\pm}$, $F^{\pm}$ are two third-order terms and a fourth-order term, respectively. As indicated in Eq. (10), the postcollision moment vector α_k^{+} can be computed from the precollision moment vector α_k^{-} (see [44] for details). For the high-order terms $T_{1,2}^{\pm}$ and $F^{\pm}$, apply $T_{1,2}^{+} = -\gamma_1 T_{1,2}^{-}$ with a free parameter γ_1 to deal with the third-order terms, and simply set $F^{+} = 0$ for the fourth-order term.

As shown above, the collision process of the FMLB model is implemented in the moment space, which has been proven to be similar to that of the standard MRT model in our previous work [47]. Indeed, with the assumption of $B = 1$, the present FMLB model can be viewed as a special case (two-relaxation-time) of the MRT model with the trapezoidal rule (see Appendix A for details).

B. Effective viscosity

Viscosity in gases is an inherent physical property and arises principally from the molecular diffusion that transports momentum between gas molecules, which is a very critical parameter in the numerical simulations of real gas flows. In the simulation of continuum flows, the viscosity can be determined by the most important characteristic parameter, namely the Reynolds number (Re). For the noncontinuum flows, e.g., microscale gas flows, the most important characteristic parameter of the flow is the Knudsen number (Kn). Thus, as pointed out in Refs. [22,26,35], the relation between the viscosity or relaxation parameter(s) in the LB models and the Knudsen number should be given appropriately for the simulations of microscale gas flows.

From gas kinetic theory [48], the mean free path λ is related to the dynamic viscosity $\mu = \rho\nu$, the macroscopic pressure p, and temperature T, and can be expressed as

$$\lambda = \frac{\mu}{p}\sqrt{\frac{\pi RT}{2}}. \tag{11}$$

For the isothermal D2Q9 LB models, according to Eq. (11) and the equation of state $p = \rho c_s^2$, the kinematic viscosity can be determined from the Knudsen number as

$$\nu = \frac{1}{3}\sqrt{\frac{6}{\pi}}\mathrm{Kn}N\delta_x, \tag{12}$$

where $N = H/\delta_x$ is the lattice number in the characteristic length. Note that the fact that $c = \sqrt{3}c_s = \sqrt{3RT} = \delta_x/\delta_t = 1$ for the D2Q9 model has been used in the deduction. Because the dynamic viscosity of a real monatomic gas is independent of density, for a specific gas and fixed characteristic length, Eq. (12) indicates that the local kinematic viscosity is proportional to the local Knudsen number, and it also implies that the local Knudsen number is inversely proportional to the local density for a constant μ.

For microscale gas flows over a solid wall, the collisions between gas molecules are not sufficient due to the wall confinement effects [26], especially in the near-wall region. Thus, there exists a so-called Knudsen layer near the wall and its thickness is in order of the mean free path. Within the Knudsen layer, it can be expected that the local mean free path is much smaller than that in a system without a wall. For microflows with a large Kn, e.g., in the transition flow regime, the effects of the Knudsen layer become very important. Therefore, incorporating the wall effects on the microflow into the LBM framework is necessary and helpful to improve its capability for simulating microchannel gas flows. Following the literature, the effects of the Knudsen layer can be introduced into the present LBM framework via using the effective mean free path, which is equivalent to making use of the effective Knudsen number or effective viscosity.

In this study, we adopt the Bosanquet-type effective viscosity in the form [41]

$$\mu_e = \frac{\mu}{1 + a\mathrm{Kn}}, \tag{13}$$

where a is the rarefaction parameter. Beskok and Karniadakis [41] first applied this expression and used $a = 2.2$ in the simulations of microchannel flows in the transition regime. In later years, another choice, $a = 2$, was suggested by some other researchers [37,43,49]. Noted that the Bosanquet-type effective viscosity is independent of the distance from the wall and only related to the local Knudsen number, which implies it is not the real local effective viscosity, and just the overall confinement effects are considered in the numerical simulations. In the work of Michalis *et al.* [43], this overall rarefaction effect on gas viscosity was investigated in detail through the DSMC simulations of isothermal, low-speed flows in a long microchannel, in which the average values of the viscosity over a cross section were considered, and then the relationship between the cross-sectional average viscosity and the Knudsen number within the same channel was investigated. It was noteworthy that Michalis *et al.*'s study showed that the rarefaction parameter a is not constant and also depends on the Kn value, but this dependence was rather weak over the majority of the transition regime, suggesting an "effective" value close to 2. Recently, this Bosanquet-type effective viscosity with $a = 2$ has been successfully applied to the LBGK and MRT models for microchannel gas flows in the transition regime [37,39].

In the present FMLB simulations, we define an effective kinematic viscosity with $a = 2$ based on Eqs. (12) and (13) as

$$\nu_e = \frac{1}{3}\sqrt{\frac{6}{\pi}}\frac{\mathrm{Kn}N\delta_x}{1 + a\mathrm{Kn}}. \tag{14}$$

III. KINETIC BOUNDARY CONDITION FOR THE FMLB MODEL

As is well known, an appropriate boundary condition is always one of the critical points in the numerical simulations using the LB models, especially for the applications in microscale gas flows. To our knowledge, two widely used kinetic boundary conditions have been proposed for the BGK- and MRT-LB models in the literature, namely the discrete Maxwellian boundary conditions (DMBC) [16,18] and the combined bounce-back and specular-reflection (CBBSR) boundary condition [50]. Through detailed analysis on the two boundary conditions for the BGK- and MRT-LB models, respectively, given by Guo *et al.* [22] and Guo and Zheng [51], the discrete effects were reported to be existing in the two kinds of LB models, and the CBBSR schemes within both LB models were found to be identical in a parametric range; also, their analysis indicated that the CBBSR scheme has a wider parameter range than that of the DMBC scheme, which means the CBBSR scheme can be applied for a wider slip velocity range than the DMBC ones. As reported in the literature, the key to simulating microscale gas flows using the LB models is how to correct the intrinsic unphysical discrete effects to implement an exact slip boundary condition.

In this study, the CBBSR scheme is applied for the present FMLB simulations, as illustrated in Fig. 1. If boundary conditions are imposed at position $\vec{x} + \vec{c}_i\delta_t/2$, then $\vec{c}_{\bar{i}} = -\vec{c}_i$ and $\vec{c}_{i'} = \vec{c}_i - 2(\vec{c}_i \cdot \vec{n})\vec{n}$ ($\vec{n}$ is the unit normal vector), respectively, are the opposite and specular velocity of $\vec{c}_i$; the unknown distribution $N_i(\vec{x} + \vec{c}_i\delta_t/2, t + \delta_t/2)$ entering the fluid domain at that point can be computed as follows:

$$\begin{aligned} &N_i\left(\vec{x} + \frac{\vec{c}_i\delta_t}{2}, t + \frac{\delta_t}{2}\right) \\ &\quad = rN_{\bar{i}}\left((\vec{x} + \vec{c}_i\delta_t) + \frac{\vec{c}_{\bar{i}}\delta_t}{2}, t + \frac{\delta_t}{2}\right) \\ &\qquad + (1 - r)N_{i'}\left([\vec{x} + (\vec{c}_i \cdot \vec{n})\vec{n}\delta_t] + \frac{\vec{c}_{i'}\delta_t}{2}, t + \frac{\delta_t}{2}\right), \end{aligned} \tag{15}$$

where $r \in [0,1]$ is the portion of the bounce-back part in the combination. According to Eq. (15), the CBBSR scheme on the bottom wall for the D2Q9 model (see Fig. 1) can be

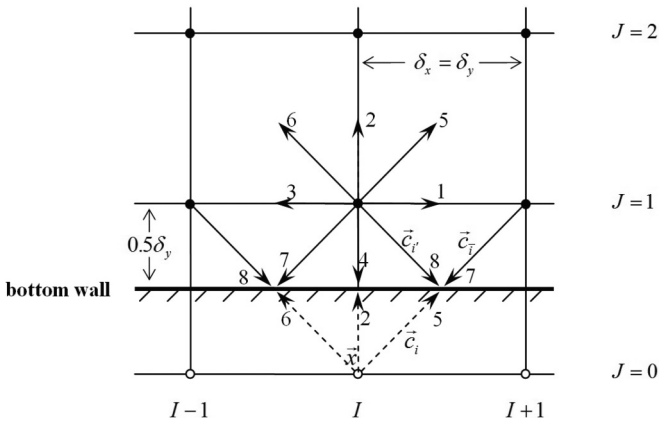

FIG. 1. Schematic diagram of the CBBSR scheme in the D2Q9 model.

expressed as

$$\begin{aligned} N_{2,I}^{0+} &= N_{4,I}^{1+}, \\ N_{5,I}^{0+} &= rN_{7,I+1}^{1+} + (1-r)N_{8,I}^{1+}, \\ N_{6,I}^{0+} &= rN_{8,I-1}^{1+} + (1-r)N_{7,I}^{1+}, \end{aligned} \tag{16}$$

where the dependence on $(\vec{x} \pm \vec{c}_i\delta_t/2, t \pm \delta_t/2)$ is dropped for notation simplicity, e.g., the distribution functions $N_i(\vec{x} \pm \vec{c}_i\delta_t/2, t \pm \delta_t/2)$ for the node at index of $(I, J = 0)$ have been simplified as $N_{i,I}^{0\pm}$.

As reported in the literature [22,26,51], when the CBBSR scheme is used to represent the slip boundary conditions within the LBM framework, the parameter r plays an important role in the simulations of microflows, which must be corrected accurately to realize the exact slip boundary conditions, and the corrected formulations are different for the different LB models due to its different discrete effects. In the following subsection, we first analyze the discrete effects of the CBBSR scheme within the FMLB model and then present the corrected bounce-back portion r to realize an exact prescribed slip boundary condition.

A. Analysis of the CBBSR scheme within the FMLB model

Inspired by the analysis of the CBBSR scheme in the MRT model [26,51], we consider a steady unidirectional incompressible Poiseuille flow driven by a constant force $\vec{f} = (\rho a, 0)^{\mathrm{T}}$, and we assume

$$\rho = \text{const}, \quad u_y = 0, \quad \frac{\partial \phi}{\partial t} = \frac{\partial \phi}{\partial x} = 0 \tag{17}$$

for any flow variable ϕ. Under such conditions and with the collision equation in moment spaces Eq. (A1) taken into account, substituting the second-order Taylor expansions of $N_i(\vec{x} \pm \vec{c}_i\delta_t/2, t \pm \delta_t/2)$ into the left-hand side of evolution equation (1) leads to

$$\partial_y(c_{iy}N_i) = \Omega_i(N) = -[\boldsymbol{E}^{-1}\boldsymbol{\Lambda}(\boldsymbol{\alpha}^{-} - \boldsymbol{\alpha}^{\mathrm{eq}})]_i. \tag{18}$$

Then, multiplying Eq. (18) by c_{ix} and subsequently summing over all i while utilizing the related expressions and symmetry properties, we can obtain the following equation:

$$-\frac{\partial}{\partial y}\left(\nu \frac{\partial u_x}{\partial y}\right) = a. \tag{19}$$

This indicates that, under this condition, the evolution equation in the FMLB model, Eq. (1), is actually a second-order numerical scheme of the exact Navier-Stokes equation for this Poiseuille flow.

To investigate the discrete error introduced by the CBBSR scheme, according to the procedures proposed in Ref. [26], we can obtain the following relation between the horizontal velocities at node indexes of $J = 1$ and 2 (cf. Fig. 1):

$$\begin{aligned} u_2 = &\left(1 + \frac{2r(1-G)}{1+G-2rG}\right)u_1 - \frac{1-G}{1+G-2rG} \\ &\times \left[6 - r\left(\frac{6G}{1+G} + \frac{1+5\gamma_1}{1+\gamma_1}\right)\right]\delta_t a, \end{aligned} \tag{20}$$

where $u_{1,2} = u_x|_{J=1,2}$ and $G = (6\nu - \delta_t)/(6\nu + \delta_t)$. More details of this deduction are provided in Appendix B.

For the Poiseuille flow considered in the present study, with an additional constraint $\partial u_x/\partial y|_{y=H/2} = 0$, we can obtain the analytical solution of the macroscopic control equation (1) in the form

$$u_j = 4u_c y_j'(1 - y_j') + u_s, \tag{21}$$

where $y_j' = (j - 0.5)\,\delta_y/H$, $u_c = 8aH^2/\nu$, and u_s is the slip velocity at the wall. Substituting the analytical solution of $u_{1,2}$ and the expression of parameter G into Eq. (20) while utilizing Eq. (12), the slip velocity at the wall produced by the CBBSR scheme can be expressed in terms of Kn as

$$U_s = \frac{u_s}{u_c} = 4\frac{1-r}{r}\sqrt{\frac{6}{\pi}}\mathrm{Kn} + \frac{1-\gamma_1}{1+\gamma_1}\frac{8}{3}\sqrt{\frac{6}{\pi}}\mathrm{Kn}\Delta - \Delta^2, \tag{22}$$

where $\Delta = 1/N = \delta_x/H$, and note that $\delta_x = \delta_t$ has been used in this deduction. This equation shows that the nondimensional slip velocity is not only influenced by the parameter r and the Knudsen number, but is also related to the numerical part depending on the grid resolution. To our knowledge, when $r = 1$ the CBBSR scheme is reduced to the no-slip bounce-back scheme, but Eq. (22) shows that the slip velocity still exists, $U_s = \frac{1-\gamma_1}{1+\gamma_1}\frac{8}{3}\sqrt{\frac{6}{\pi}}\mathrm{Kn}\Delta - \Delta^2$; fortunately, similar to the treatment in the MRT model [26], for the purely bounce-back rule, the numerical slip velocity can be eliminated by setting the free parameter $\gamma_1 = (8\nu - \delta_x)/(8\nu + \delta_x)$. In addition, the most important point is that, similar to the results reported by Guo *et al.* [22,26,51] for the cases of the LBGK and MRT models, there exist some inherent discrete effects in this kinetic boundary condition, which must be corrected to realize an exact prescribed slip boundary condition. In the following, we focus on how to correct this issue for the present FMLB model.

B. Second-order slip boundary condition

For microscale gas flows, the widely used and so-called second-order slip boundary condition can be written in the form

$$u_s = A_1\lambda \left.\frac{\partial u}{\partial y}\right|_{\text{wall}} - A_2\lambda^2 \left.\frac{\partial^2 u}{\partial y^2}\right|_{\text{wall}}, \tag{23}$$

where A_1 and A_2 are the two slip parameters and are usually determined from theory, experiments, or experiences. For the Poiseuille flow mentioned above, substituting the Navier-Stokes solution Eq. (21) into this boundary condition Eq. (23) yields a slip velocity at the wall as

$$U_s = 4A_1\mathrm{Kn} + 8A_2\mathrm{Kn}^2. \tag{24}$$

Therefore, combining Eqs. (22) and (24), we can conclude that, in order to match the expected second-order slip boundary condition, the parameter r in the CBBSR scheme must be chosen as

$$r = \left[1 + \sqrt{\frac{\pi}{6}}\left(A_1 + 2A_2\mathrm{Kn} - \frac{1-\gamma_1}{1+\gamma_1}\frac{2}{3}\sqrt{\frac{6}{\pi}}\Delta + \frac{\Delta^2}{4\mathrm{Kn}}\right)\right]^{-1}. \tag{25}$$

It can be found from this expression that the control parameters r not only depend on the predetermined parameters A_1 and A_2,

but they also relate to the Knudsen number Kn and the grid resolution (recall that $\Delta = \delta_x/H = 1/N$), which is different from the MRT results reported in the literature [26,51]. Furthermore, the influence of grid resolution can be removed by setting the free parameter $\gamma_1 = (8\nu - \delta_x)/(8\nu + \delta_x)$ in the present FMLB model.

In this study, in order to obtain the exact second-order slip boundary condition, the effects of the effective viscosity on the CBBSR scheme must also be taken into consideration. According to Eqs. (12)–(14), we can define a Bosanquet-type effective Knudsen number Kn_e as follows:

$$\mathrm{Kn}_e = \frac{\mathrm{Kn}}{1 + a\mathrm{Kn}}, \tag{26}$$

where it is clear that Kn_e and ν_e still satisfy the original relationship Eq. (12). Combining Eqs. (25) and (26), the control parameter r with the corrections from the effects of the "effective viscosity" method can be given as

$$r = \left[1 + \sqrt{\frac{\pi}{6}}\left(A_1 + 2A_2\mathrm{Kn}_e - \frac{1-\gamma_1}{1+\gamma_1}\frac{2}{3}\sqrt{\frac{6}{\pi}}\Delta + \frac{\Delta^2}{4\mathrm{Kn}_e}\right)\right]^{-1}, \tag{27}$$

in which the terms related to Δ can also be removed by setting $\gamma_1 = (8\nu_e - 1)/(8\nu_e + 1)$ and then Eq. (27) can be simplified as

$$r = \left[1 + \sqrt{\frac{\pi}{6}}\left(A_1 + 2A_2\mathrm{Kn}_e\right)\right]^{-1}. \tag{28}$$

As pointed out by Li *et al.* [37], due to the introduction of the effective mean free path, the slip coefficients A_1 and A_2 are different from that used in the original second-order slip boundary condition (e.g., $A_1 = 1.11$ and $A_2 = 0.61$ [52], $A_1 = 1.0$ and $A_2 = 0.5$ [53]) and both coefficients should be modified properly. In the MRT simulations for microchannel flows in the transition regime, Li *et al.* [37] suggested that the two slip coefficients can be chosen as

$$A_1 = \frac{2-\sigma}{\sigma}\left(1 - 0.1817\sigma\right), \quad A_2 = 0.8, \tag{29}$$

where σ is the tangential momentum accommodation coefficient (TMAC). In the literature, the *a posteriori* method was usually used to determine the slip coefficients via demonstrating the capability of predicting an accurate mass flow rate [37,52,54]. It should be noted that the results of the mass flow rate for the periodic microchannel flow obtained by Li *et al.* using the two constant slip coefficients obviously deviate from the benchmark solutions of Cercignani *et al.* at relatively large Knudsen numbers ($4 < \mathrm{Kn} \leqslant 10$). Through investigations with an adjustable second slip coefficient for the periodic microchannel flow at $4 < \mathrm{Kn} \leqslant 10$, we find that the mass flow rate obtained with a larger value of the second slip coefficient better fits the benchmark solution. Hence, in the present study, based on Li *et al.*'s suggestion, we choose the same first slip coefficient $A_1 = (1 - 0.1817\sigma)(2-\sigma)/\sigma$ and give a nonconstant second slip coefficient B_2 [see Eq. (30)], where the value of B_2 is close to $A_2 = 0.8$ at the moderate Knudsen numbers ($0.1 \leqslant \mathrm{Kn} \leqslant 2$) and increases gradually with the further increase of Kn. In the present FMLB framework with the effective viscosity, the corrected bounce-back portion r can be determined as

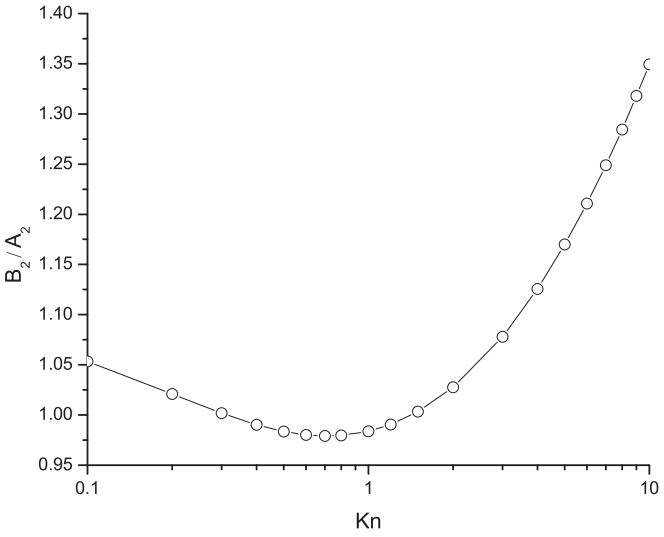

FIG. 2. The ratio of the present second slip coefficient to that suggested by Li *et al.* as a function of Kn in the transition regime

$$r = \left[1 + \sqrt{\frac{\pi}{6}}\left(A_1 + 2B_2\mathrm{Kn}_e\right)\right]^{-1}, \quad B_2 = A_2\frac{1 + a\mathrm{Kn}}{\Psi\left(\mathrm{Kn}\right)}, \tag{30}$$

where the value of A_2 is still set at 0.8, and $\Psi\left(\mathrm{Kn}\right)$ is a function of Kn. It can be found that Eq. (30) can be reduced to Eq. (28) by setting $\Psi\left(\mathrm{Kn}\right) = 1 + \bar{a}\mathrm{Kn}$ with $\bar{a} = a$. In the present study, through choosing different values of $\bar{a}$ for the different Kn, we can give a better fitting between the mass flow rate predicted by Eq. (30) and the solution of the linearized Boltzmann equation for microchannel flows in the upper transition regime. Finally, according to the discrete data of $\bar{a}$ in the tests and choosing a proper basis function, $\Psi\left(\mathrm{Kn}\right)$ can be approximated as the following fitting function:

$$\Psi\left(\mathrm{Kn}\right) \approx 3.57(1 + \mathrm{Kn})^{0.68} - 2.67. \tag{31}$$

To give a straightforward view of this fitting function, in Fig. 2 we plot the ratio of the value of B_2 to that of A_2 suggested by Li *et al.* as a function of the Knudsen number Kn in the entire transition regime, which is obtained by substituting Eq. (31) into Eq. (30) while setting $a = 2$.

IV. NUMERICAL RESULTS AND DISCUSSIONS

Microchannel gas flows with periodic or pressure boundary conditions have been studied by many researchers and employed as the benchmark cases for steady incompressible microscale gas flow. In this study, both cases are investigated using the present FMLB model with the effective viscosity method and the corrected CBBSR boundary condition, where r is determined from Eq. (28) or Eq. (30). All numerical tests performed in this study use Cartesian coordinates with a uniform gird ($\delta_x = \delta_y = 1$), the corresponding time step size is $\delta_t = 1$, and the characteristic length takes the width

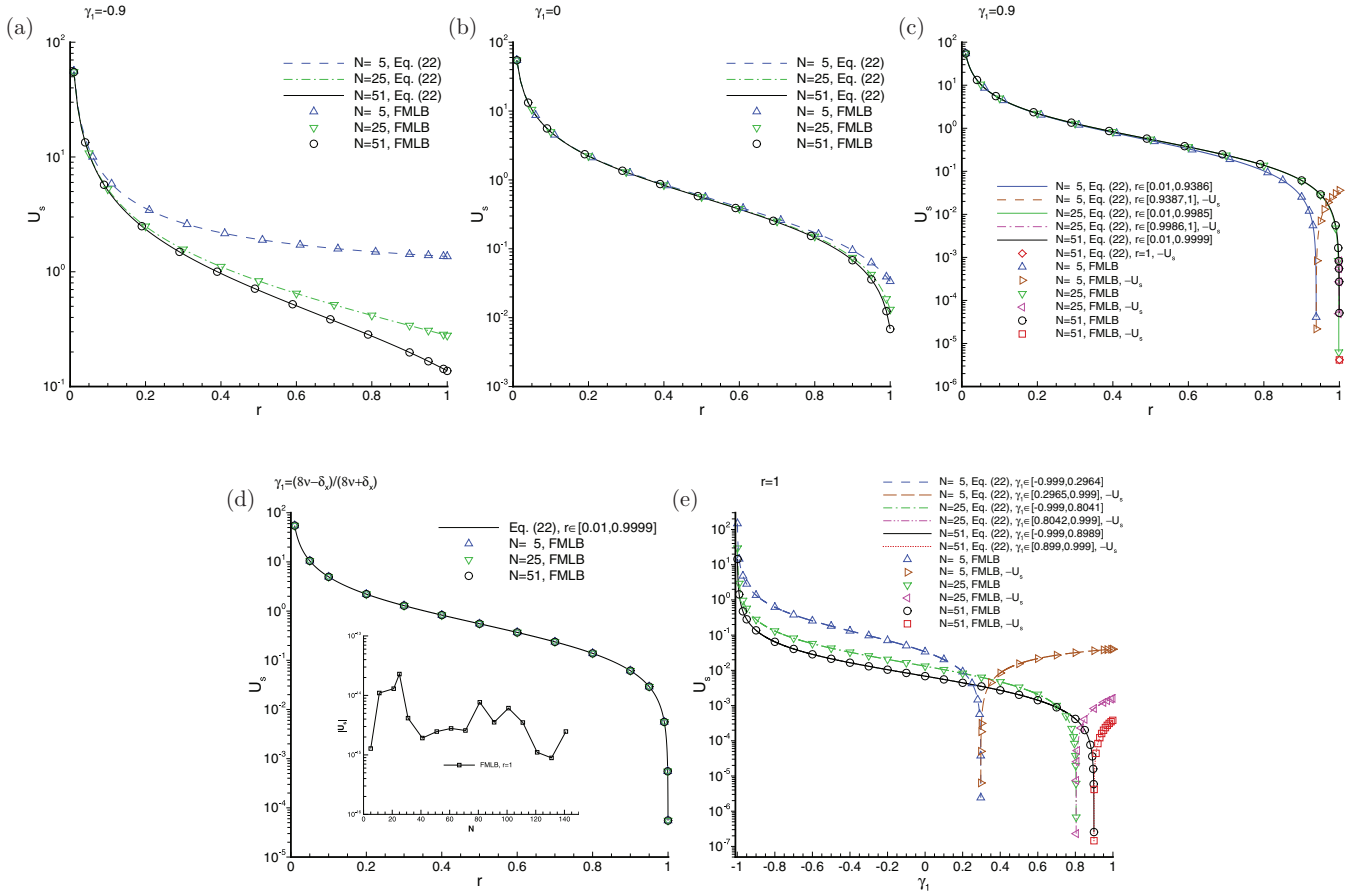

FIG. 3. (Color online) Dimensionless slip velocities as a function of γ_1 or r with different resolutions N (Kn = 0.1): (a) $\gamma_1 = -0.9$, (b) $\gamma_1 = 0$, (c) $\gamma_1 = 0.9$, (d) $\gamma_1 = (8\nu - \delta_x)/(8\nu + \delta_x)$, and (e) $r = 1$.

of the channel ($H = N\delta_y = N$). In the present simulations, the convergence criterion toward the steady state is set as follows:

$$\sqrt{\frac{\sum_i |\vec{u}(\vec{x}_i, t^n) - \vec{u}(\vec{x}_i, t^n - 1000\delta_t)|^2}{\sum_i |\vec{u}(\vec{x}_i, t^n)|^2}} < 10^{-12}. \quad (32)$$

A. Validation of the CBBSR scheme within the FMLB model

In this subsection, we carry out some numerical tests to validate our theoretical analysis in Sec. III for the CBBSR scheme within the FMLB model. It should be pointed out that, for all test cases in this validation, the effective viscosity method is not introduced.

We first perform a systematic investigation on the discrete effects of the CBBSR scheme within the present FMLB framework, including the numerical tests with the different bounce-back parameter r and the different values of free parameter γ_1, as well as the different resolutions N varying from 5 to 51. A series of force-driven Poiseuille flows in a microchannel at Kn = 0.1 are simulated by the present FMLB model. In the simulations, the fluid density is $\rho = 1$ and the constant acceleration a is set at 10^{-4}. The periodic boundary conditions are applied to the inlet and outlet of the channel, and the CBBSR scheme is applied at the two parallel walls. The present results of these test cases are classified and grouped into five plots in Fig. 3. Figures 3(a), 3(b), 3(c), and 3(d) illustrate the present simulated dimensionless slip velocities as a function of r for $\gamma_1 = -0.9$, $\gamma_1 = 0$, $\gamma_1 = 0.9$, and $\gamma_1 = (8\nu - \delta_x)/(8\nu + \delta_x)$, respectively, and Fig. 3(e) shows the present simulated dimensionless slip velocities as a function of γ_1 in the study of the purely bounce-back scheme ($r = 1$) for the no-slip boundary condition. For the purpose of comparison, those analytical results obtained by Eq. (22) are also included in those plots in Fig. 3. All present results in Fig. 3 show an excellent agreement with the analytical solutions given by Eq. (22), demonstrating the correctness of our theoretical analysis.

To further investigate the influence of the control parameters r in the CBBSR scheme on the realization of the expected slip boundary condition, and to validate the present analysis on the correction of the parameters r [see Eq. (25)], the fully diffusive case [$A_1 = 2\zeta/\sqrt{\pi} \approx 1.1466$, $A_2 = (1 + 2\zeta^2)/\pi \approx 0.9757$, with $\zeta = 1.016\,15$] that was often tested in the literature [22,23,51] is simulated by the present FMLB model at Kn = 0.2. Here, the influences of different grid resolutions are also investigated by varying the grid resolution N from 5 to 51. For the fully diffusive walls, the bounce-back fraction r is usually set to 0.5 when ignoring the discrete effects of the CBBSR scheme, while it must be computed from the

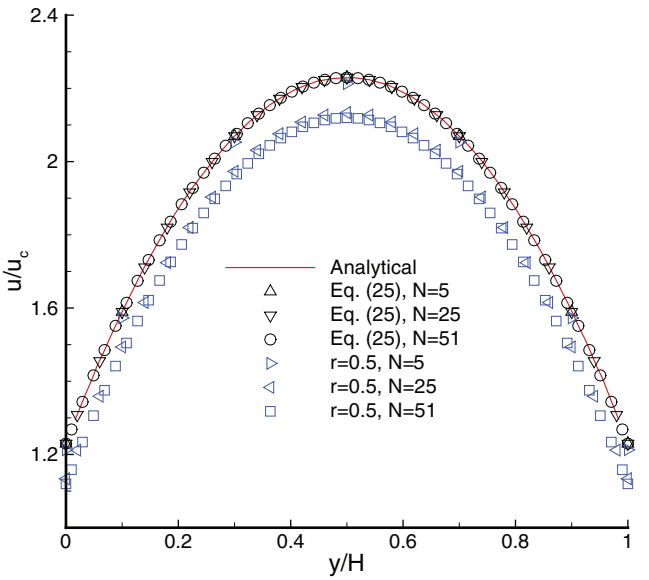

FIG. 4. (Color online) Velocity profiles for the Poiseuille flow at Kn = 0.2 for the fully diffusive walls with different grids. The analytical solution of Cercignani [48] is extracted from Fig. 4 of Ref. [22].

correction Eq. (25) to consider those discrete effects within the FMLB model. For all three chosen grids $N = 5$, 25, and 51, the velocity profiles predicted by the present FMLB model with the corrected parameter r given by Eq. (25) are plotted in Fig. 4, in which the results obtained with $r = 0.5$ are also included for comparison purposes. It can be seen that all of the present results obtained with the corrected parameter r are in excellent agreement with the analytical solution reported by Cercignani [48], but for those results with $r = 0.5$, the grid-dependent deviations from the benchmark solution can be clearly observed. As revealed in Fig. 4, there are inherent discrete effects existing in the CBBSR scheme for the FMLB model, and it is necessary to correct r in order to accurately realize the slip boundary condition for the microscale gas flow.

B. Microchannel flows with the periodic boundary condition

Gas flow in a microchannel with a periodic or pressure boundary condition has been investigated by many researchers using the LBGK and MRT models and employed as the benchmark cases of steady incompressible microscale gas flow (cf. Refs. [26,35,37,38,40]). In this subsection, we apply the present FMLB model with the Bosanquet-type effective viscosity to study the periodic microchannel flow driven by a constant force. Here, all simulations are performed on a uniform grid ($N_x \times N_y = 51 \times 51$), and the driven force is set as $f_x = \rho a = 10^{-4}$. The periodic boundary condition is applied at the inlet and outlet of the channel, and the CBBSR boundary condition with the fitting function Ψ (Kn) is applied at the top and bottom walls, which are assumed to be fully diffusive ($\sigma = 1$). Figure 5 shows the velocity profiles normalized by the mean velocity over the cross section of the channel $\bar{u} = (1/H)\int_0^H u\,dy$ at $\mathrm{Kn} = 2k/\sqrt{\pi}$, with k ranging from 0.1 to 10. The numerical results obtained by Guo *et al.* [26] and Li *et al.* [37] using the MRT models, respectively, with Stops' expression of effective viscosity and the Bosanquet-type effective viscosity, as well as the benchmark solutions of the linearized Boltzmann equation given by Ohwada *et al.* [55], are also grouped in Fig. 5 for comparison purposes. Noted that, as reported in the literature [26,37], the solutions of the Navier-Stokes equations with the second-order slip boundary conditions [48,52] are increasingly deviating from the linearized Boltzmann results with increasing Kn beyond 0.1128, so the slip-NS results are not presented again in Fig. 5. It can be clearly seen from Fig. 5 that the velocity profiles predicted by the present FMLB model with the fitting function Eq. (30) and those MRT solutions given by Li *et al.* [37] are almost the same for Kn varying from 0.1128 to 4.5135, and both results are in good agreement with the linearized Boltzmann solutions; the MRT results given by Guo *et al.* using Stops' expression of effective viscosity show a visible deviation from the benchmark solution as $\mathrm{Kn} \geqslant 1.1284$. For larger Knudsen numbers Kn = 6.7703, 9.0270 and 11.2838 ($k = 6$, 8, and 10), the velocity profiles were not given in the studies of Guo *et al.* [26] and Li *et al.* [37], but the velocity profiles predicted by the present FMLB model with Eq. (30) are presented here and also agree well with the solutions of the linearized Boltzmann equation, as shown in Fig. 5. To investigate the influence of the fitting function Ψ (Kn) used in the corrected CBBSR scheme [see Eqs. (30) and (31)], the present results at the four relatively large Knudsen numbers Kn = 4.5135, 6.7703, 9.0270, and 11.2838, which are obtained with the constant slip coefficients suggested by Li *et al.*, Eq. (28), are also plotted in Fig. 5. The comparisons between the two group results and the benchmark solutions show that, in the present FMLB frameworks, using the fitting function Eq. (30) can yield a slightly better match for the velocity profile at relatively large Kn in the transition regime.

To further validate the present model, in Fig. 6 we plot the nondimensional mass flow rate $Q = \int_0^H \rho u\,dy$ normalized by $\rho a H^2/\sqrt{2RT}$ against the Knudsen number. It can be found from Fig. 6 that the mass flow rate predicted by the present FMLB model with Eq. (30) is almost identical to the solution of the MRT model given by Li *et al.* [37], because the same effective viscosity and the same second-order slip boundary condition are used in the two models, and both models can only provide reasonable results up to $\mathrm{Kn} \approx 3$. However, when taking the fitting function Ψ (Kn) into consideration, the present model with Eq. (30) can provide a satisfactory mass flow rate for the entire transition flow regime (up to $\mathrm{Kn} \sim 10$) in comparison with the solution of the Boltzmann equation given by Cercignani *et al.* [48]. The comparisons between the two present results with and without the fitting function show that the second-order slip term in the boundary condition plays an important role in simulating rarefied gas flows with relatively large Knudsen numbers, and the present FMLB model with the effective viscosity can be extended to simulate microchannel flow at a relatively larger Knudsen number by making appropriate fixes in the slip boundary conditions. Besides, the well-known Knudsen minimum phenomena are all observed for those results obtained by different methods, which is captured at $\mathrm{Kn} \approx 0.9$ for both of the present results.

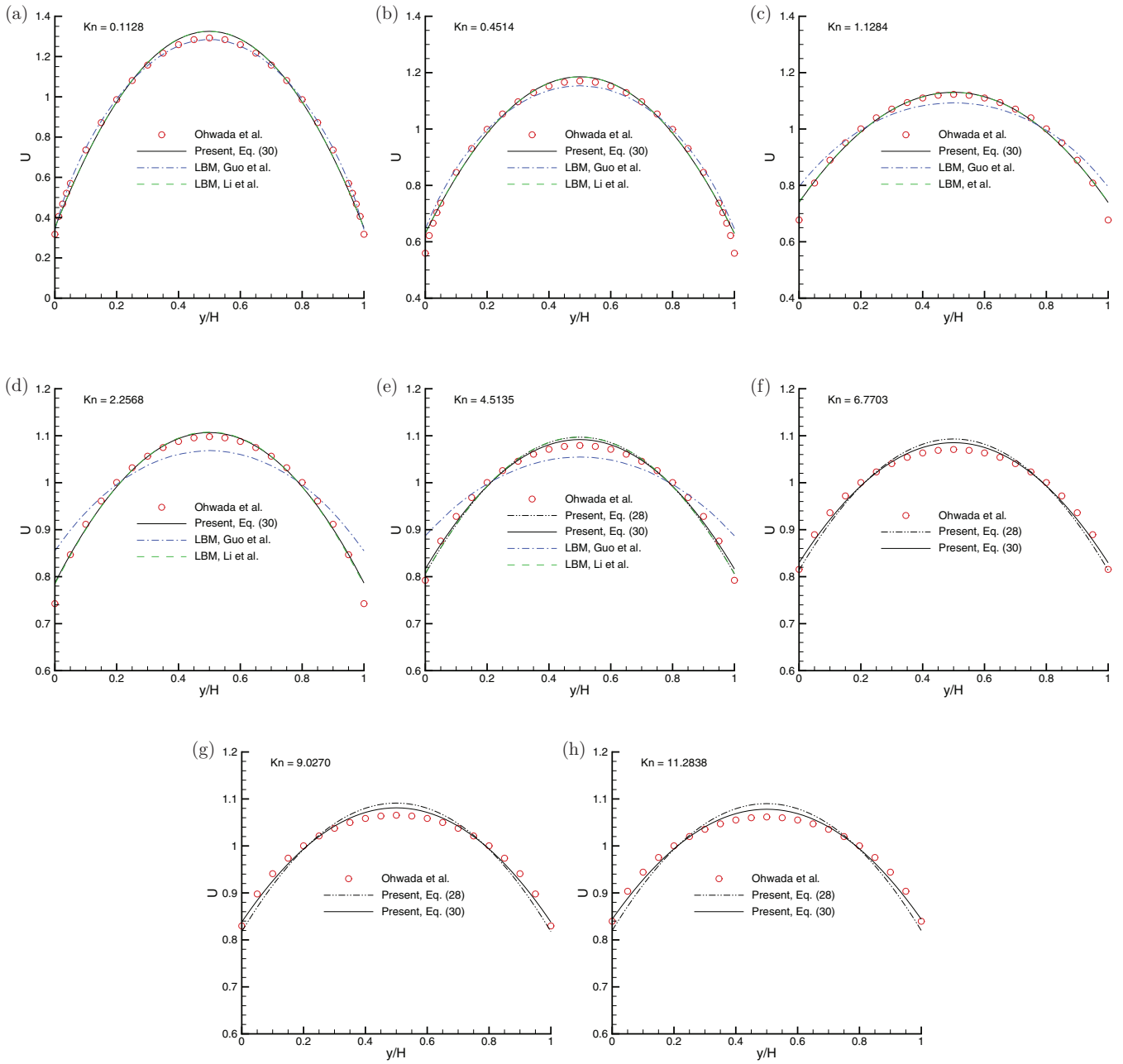

FIG. 5. (Color online) Velocity profiles of gas flow in a periodic microchannel ($U = u/\bar{u}$).

C. Microchannel flows with the pressure boundary condition

The present FMLB model is also applied to simulate pressure-driven gas flow in a long microchannel, which is a basic phenomenon and has wide engineering applications in MEMS. In this problem, the flow is driven by the substantial drops between the pressures at the inlet and outlet of the channel, and the pressure distribution along the microchannel is usually nonlinear [27,37,40]. Following the literature, in this study the ratio of the length to the height of the channel is set to be $L/H = 100$, and the pressure at the inlet and at the outlet is set to be p_{in} and p_{out}, respectively. In our simulations, the outlet density is set to be $\rho_{\text{out}} = 1$; to keep the dynamic viscosity constant along the channel, the local Knudsen number is inversely proportional to the local density and varies along the channel, $\text{Kn}(x) = \text{Kn}_{\text{out}}\rho_{\text{out}}/\rho(x)$, where the local density $\rho(x)$ takes the value at the centerline of the channel and Kn_{out} is the Knudsen number at the outlet.

Throughout the numerical experiments presented in this section, a 2100×21 uniform grid is adopted and the top and bottom walls are still assumed to be fully diffusive ($\sigma = 1$) unless otherwise notified, where the CBBSR scheme with the fitting function is applied. The consistent linear extrapolation scheme [24,40] is used to realize the pressure boundary condition at the inlet and outlet, in which the densities at the inlet and outlet are renormalized so that the average densities satisfy the pressure boundary conditions, and this

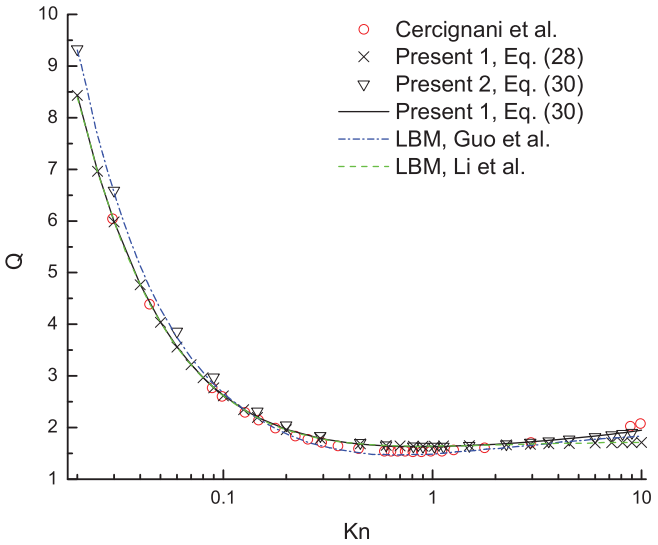

FIG. 6. (Color online) Nondimensional mass flow rate against the Knudsen number for microchannel gas flow. Present 1: for the periodic case; Present 2: for the pressure-driven case.

treatment can ensure the smooth transition of the pressure and velocity fields from the interior nodes to the boundary. The details of the implementation procedure can be found in the literature [40].

For the pressure-driven microchannel flows, we first consider the following two cases ranging from the slip flow regime to the transition regime: (i) $\mathrm{Kn}_{\mathrm{out}} = 0.0194$, $p_{\mathrm{in}}/p_{\mathrm{out}} = 1.4$; (ii) $\mathrm{Kn}_{\mathrm{out}} = 0.388$, $p_{\mathrm{in}}/p_{\mathrm{out}} = 2$, which have been investigated using different numerical methods in the literature [26,37,56,57]. In Figs. 7 and 8, the nondimensional streamwise velocity $u/u_{\max}$ at the outlet and the pressure deviation $\delta p = (p - p_l)/p_{\mathrm{out}}$ along the centerline of the channel are presented for the above three cases. Here, $u_{\max}$ is the maximum velocity at the outlet, and $p_l(x) = p_{\mathrm{in}} + x(p_{\mathrm{out}} - p_{\mathrm{in}})/L$ is the linear profile of the pressure along the centerline. It should be pointed out that the DSMC and IP-DSMC results of Shen *et al.* [56], the analytical results of Arkilic *et al.* [57] obtained by the NS equations with the first slip boundary condition, as well as the MRT results (for the later two cases) reported by Li *et al.* [37] are also grouped in those plots in Figs. 7 and 8 for comparison purposes.

For $\mathrm{Kn}_{\mathrm{out}} = 0.0194$ and $p_{\mathrm{in}}/p_{\mathrm{out}} = 1.4$, both profiles of velocity and pressure deviation predicted by the present FMLB model agree well with those of the DSMC, IP-DSMC, and Slip-NS methods, as shown in Fig. 7. When $\mathrm{Kn}_{\mathrm{out}}$ increases up to 0.388 and $p_{\mathrm{in}}/p_{\mathrm{out}} = 2$, the whole flow field falls into the transition flow regime; it can be observed from Fig. 8 that both results of the velocity profile and pressure deviation given by the slip-NS method show significant deviations from those benchmark solutions of the DSMC and IP-DSMC methods, while both results predicted by the present model with the effective viscosity also agree fairly well with the benchmark solutions, which confirms that it is necessary to take the effects of the Knudsen layer into consideration for the simulations of microscale gas flow in the transition regime. Also, it can be clearly seen from Fig. 8 that both results predicted by the FMLB model with the Bosanquet-type effective viscosity

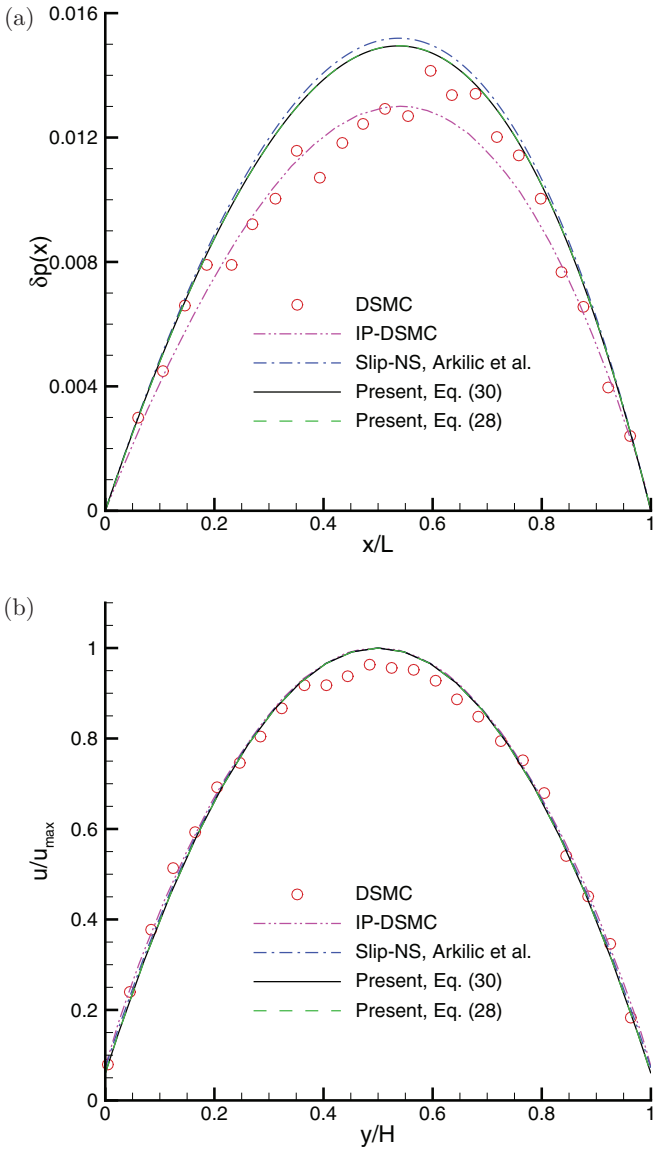

FIG. 7. (Color online) Pressure deviation along the channel centerline (a) and streamwise velocity at the outlet (b) for the pressure-driven flow in a long microchannel with $\mathrm{Kn}_{\mathrm{out}} = 0.0194$ and $p_{\mathrm{in}}/p_{\mathrm{out}} = 1.4$.

and the fitting function are in fairly good agreement with those obtained by the MRT model with the same effective viscosity method in Li *et al.*'s study [37], although different second slip coefficients are used in the second-order slip boundary conditions for the CBBSR scheme within the two different LB models. The above comparisons demonstrate that by using the corrected CBBSR scheme with the fitting function $\Psi(\mathrm{Kn})$, the present FMLB model is still able to accurately capture the characteristics of the pressure-driven flow in a long microchannel in the slip and slight transition regimes.

To further investigate the capability of the present model, pressure-driven microchannel flows with larger Knudsen numbers are also simulated in this study, and the predicted mass flow rate is compared with the benchmark solutions of the Boltzmann equation given by Cercignani *et al.* [58] and the ex-

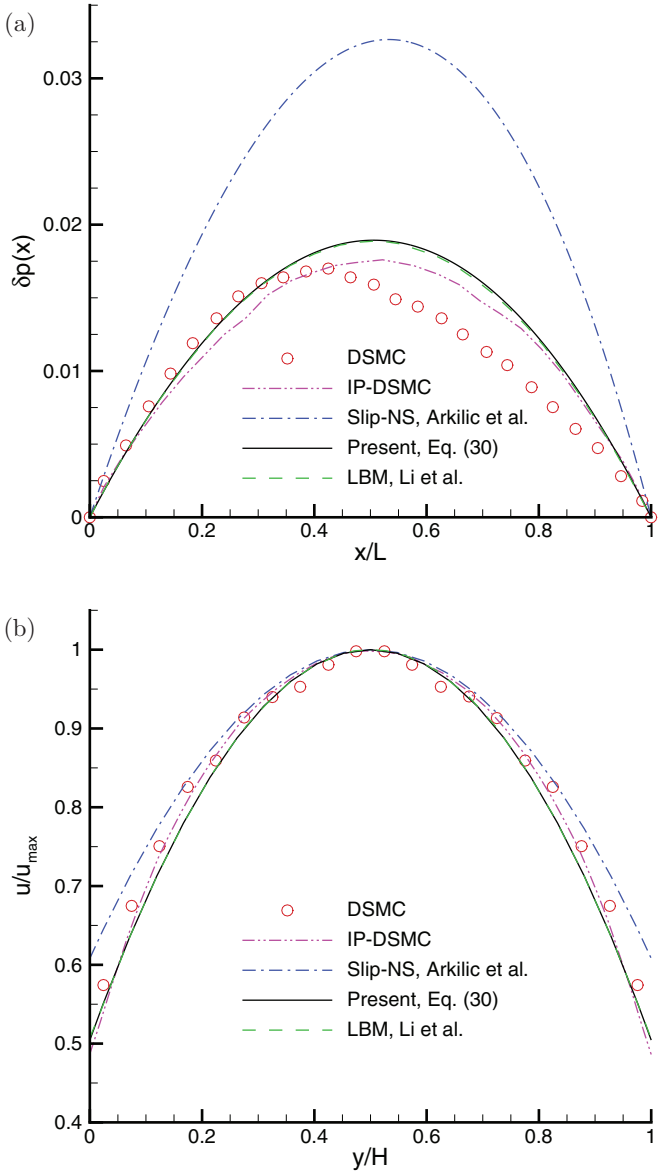

FIG. 8. (Color online) Same as Fig. 7 but for $\mathrm{Kn}_{\mathrm{out}} = 0.388$ and $p_{\mathrm{in}}/p_{\mathrm{out}} = 2$.

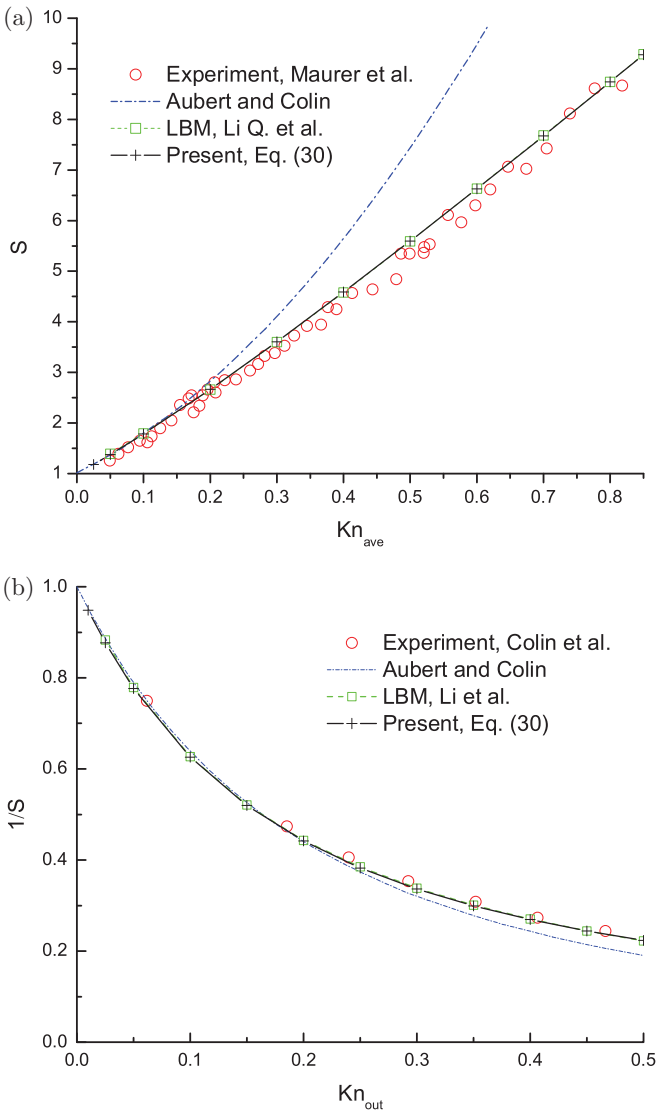

FIG. 9. (Color online) Nondimensional mass flow rate for the pressure-driven flow in a long microchannel compared with the experimental data of (a) Maurer *et al.* [59] and (b) Colin *et al.* [54,60], the solutions of Aubert and Colin's second-order slip model [61], and the MRT results of Li *et al.* [37].

perimental results for helium flows [54,59,60]. First, for comparing to the solutions of the linearized Boltzmann equation, the normalized mass flow rate $Q_{x=L/2}/(\rho a H^2/\sqrt{2RT})$ against the average Knudsen number $\mathrm{Kn}_{\mathrm{ave}} = (\mathrm{Kn}_{\mathrm{in}} + \mathrm{Kn}_{\mathrm{out}})/2$ is also plotted in Fig. 6. Here, the present results for this pressure-driven case are taken from the simulation with $p_{\mathrm{in}}/p_{\mathrm{out}} = 2$ and $\sigma = 1$, which are denoted by "Present 2, Eq. (30)" in Fig. 5. It can be found that, for this case, the present model with Eq. (30) can still give reasonable results in comparison with the benchmark data and our solutions obtained for the periodic case. Also, it should be pointed out that, for the Knudsen minimum phenomenon, there exists a small difference between both of the present results for the periodic and pressure-driven cases: it is captured at $\mathrm{Kn} \approx 0.9$ for the former case, while it occurs at $\mathrm{Kn} \approx 1$ for the latter one.

Next, following Li *et al.*'s study [37], the rarefaction effect on mass flow rate is also investigated by comparing the present results with the experimental data for helium gas reported by Maurer *et al.* [59] and Colin *et al.* [54,60]. In the following comparisons, the nondimensional mass flow rate is defined as $S = Q/Q_{\mathrm{NS}}$, where Q_{NS} represents the corresponding mass flow rate without rarefaction effects, which is obtained from the present simulations with the no-slip boundary condition [$r = 1$, $\gamma_1 = (8\nu - \delta_x)/(8\nu + \delta_x)$]. Also, to compare the present results with the solutions of Li *et al.* [37], in our computations, the TMAC is set to be $\sigma = 0.93$ and the pressure ratio $p_{\mathrm{in}}/p_{\mathrm{out}}$ is taken as 1.8.

In Figs. 9(a) and 9(b), the nondimensional mass flow rate S and the inverse one $1/S$ are shown as a function of the average and outlet Knudsen numbers, respectively. Here, not only are the experimental results of Maurer *et al.* [59] and Colin *et al.* [54,60] included, but also Li *et al.*'s results [37] obtained by the MRT model with the Bosanquet-type effective viscosity

and the solutions of Aubert and Colin's second slip model [61] are included for comparison purposes. It can be found from Fig. 9(a) that, as reported by Li *et al*. [37], Aubert and Colin's second-order slip model can only predict an accurate mass flow rate up to $\mathrm{Kn}_{\mathrm{ave}} \approx 0.18$ (corresponding to $\mathrm{Kn}_{\mathrm{out}} \approx 0.23$) when compared with the experimental data of Maurer *et al*. [59]. However, the present model can always predict fairly accurate results for all chosen Knudsen numbers ($0.05 \leqslant \mathrm{Kn}_{\mathrm{ave}} \leqslant 0.8$), as shown in Fig. 9(a). In Fig. 9(b), a similar phenomenon can also be observed. Compared with the experimental data of Colin *et al*. [54,60], the separation point for the results of Aubert and Colin [61] is show to be $\mathrm{Kn}_{\mathrm{out}} \approx 0.24$, while the present model still gives a satisfactory prediction up to $\mathrm{Kn}_{\mathrm{out}} = 0.5$. In addition, it is noteworthy that, as shown in Fig. 9, the agreement between the present solutions predicted using the FMLB model and the MRT solutions of Li *et al*. looks fairly satisfactory, although the fitting function used in this study gives a variable second slip coefficient while the fixed one was adopted in Li *et al*.'s study.

V. CONCLUSIONS

In this paper, we proposed an extended filter matrix lattice Boltzmann (FMLB) model for microchannel gas flow in which wall-confinement effects are considered. A kinetic boundary condition (CBBSR) that combines the bounce-back and specular-reflection schemes is proposed for the present FMLB model, and it is analyzed based on a unidirectional flow. The present analysis shows that the bounce-back portion r in the CBBSR boundary condition must be corrected for the present FMLB model to realize the exact prescribed boundary conditions, whether they are no-slip or slip schemes, e.g., the discrete error in the no-slip case can be eliminated via choosing an appropriate free parameter $\gamma_1 = (8\nu - \delta_x)/(8\nu + \delta_x)$, which is similar to the treatment in the case for the MRT model; to realize the specified second-order slip boundary condition, the control parameter r should be corrected according to the two slip coefficients A_1 and A_2 and the Knudsen number.

To take account of the wall-confinement effects on gas viscosity, the Bosanquet-type effective viscosity, in which the mean value of the viscosity is considered, is incorporated into the framework of the FMLB model in this study. Also, we propose a modified second-order slip boundary condition with a fitted second-order coefficient as a function of the local Knudsen number to give a satisfactory result of the mass flow rate for the high-Kn microchannel gas flow. In this work, we have implemented the present extended FMLB model to simulate the microchannel gas flows with a wide range of Knudsen numbers covering from the slip regime up to the entire transition regime. For all test cases conducted in this study, including the microchannel flow with the periodic boundary condition and the pressure-driven microchannel flow, the present FMLB results, including the velocity profile and the mass flow rate, as well as the nonlinear pressure distribution only, for the pressure-driven case, are found to be in quite good agreement with the solutions of the linearized Boltzmann equation, the results of the DSMC and IP-DSMC methods, the available experimental results, and the MRT results reported in previous studies. In particular, we also investigate the influence of the proposed fitting function on the numerical results of the mass flow rate, and the results obtained by the present extended FMLB model with the constant slip coefficients suggested in Li *et al*.'s study are also presented for comparison purposes. Those comparisons show that, for microchannel flows at low and moderate Knudsen numbers, the present FMLB model with the fitting function can give almost the same results as that with the fixed slip coefficient of Li *et al*.; the former can give satisfactory results over almost the entire transition flow regime, while the latter give the same results as those of the MRT-LB model reported by Li *et al*., which can only provide reasonable results up to $\mathrm{Kn} \approx 3$. In addition, the Knudsen minimum phenomenon is also well captured in all the simulations of both kinds of cases in this study.

Through this study, the present FMLB model has shown, in general, noticeably good accuracy and robustness for isothermal microchannel gas flows in the slip and transition regime, as indicated by various demonstrated comparisons. It looks promising for more extensive applications of the present FMLB method to other more challenging simulation scenarios in the future, e.g., the nonisothermal rarefied gas flows involving curved boundaries.

ACKNOWLEDGMENTS

C. Zhuo is grateful to Xiuliang Liu and Zhenhua Chai for some helpful discussions. This project was financially supported by the Doctorate Foundation of Northwestern Polytechnical University (Grant No. CX201209), the Aeronautical Science Fund of China (Grant No. 20111453012), as well as the National Pre-Research Foundation of China (Grant No. 9140A13040111HK0329).

APPENDIX A: THE COMPARISON BETWEEN THE FMLB MODEL AND THE MRT MODEL WITH THE TRAPEZOIDAL RULE

To simplify the analysis and without loss of generality, we consider the isothermal D2Q9 LB models. For the FMLB model, when the parameter B is fixed at 1 and taking an external force term into account, the collision process can be implemented in the moment space (see [47] for details):

$$\boldsymbol{\alpha}^{+} = \boldsymbol{\alpha}^{-} - \delta_t \boldsymbol{\Lambda}(\boldsymbol{\alpha}^{-} - \boldsymbol{\alpha}^{\mathrm{eq}}), \tag{A1}$$

with a non-negative diagonal matrix

$$\begin{aligned}\boldsymbol{\Lambda} = \mathrm{diag}(&0, 2/\delta_t, 2/\delta_t, (3\nu + \delta_t/2)^{-1}, (3\nu + \delta_t/2)^{-1},\\ &(3\nu + \delta_t/2)^{-1}, (\gamma_1 + 1)/\delta_t, (\gamma_1 + 1)/\delta_t, 0).\end{aligned} \tag{A2}$$

In Eq. (A1), $\boldsymbol{\alpha}^{\mathrm{eq}}$ denotes the equilibrium moment vector corresponding to the equilibrium distribution functions N_i^{eq}, and it can be expressed as

$$\begin{aligned}\alpha_k^{\mathrm{eq}} &= E_{ki} N_i^{\mathrm{eq}}\\ &= (\rho, \rho u_x, \rho u_y, 3\rho u_x u_x, 3\rho u_x u_y, 3\rho u_y u_y, 0, 0, 0)^{\mathrm{T}}.\end{aligned} \tag{A3}$$

Next, we start the MRT formulations from the discrete velocity Boltzmann equation (DVBE):

$$\frac{\partial N_i}{\partial t} + \vec{c}_i \cdot \vec{\nabla} N_i = \Omega_i' + F_i, \tag{A4}$$

where Ω_i' is the collision operator, and F_i is the external force term accounting for a body force $\vec{f}$.

Integrating the DVBE (A4) along the characteristic line with a time step δ_t, we obtain

$$N_i(\vec{x}+\vec{c}_i\delta_t, t+\delta_t) - N_i(\vec{x},t) = \int_0^{\delta_t} [\Omega'_i(\vec{x}+\vec{c}_i t', t+t') + F_i(\vec{x}+\vec{c}_i t', t+t')]dt'. \tag{A5}$$

For the remaining integration on the right-hand side, we approximate it by the trapezoidal rule to yield a second-order accurate but implicit in time equation,

$$N_i(\vec{x}+\vec{c}_i\delta_t, t+\delta_t) - N_i(\vec{x},t) = \frac{\delta_t}{2}[\Omega'_i(\vec{x},t) + F_i(\vec{x},t)] + \frac{\delta_t}{2}[\Omega'_i(\vec{x}+\vec{c}_i\delta_t, t+\delta_t) + F_i(\vec{x}+\vec{c}_i\delta_t, t+\delta_t)]. \tag{A6}$$

Following He *et al*. [62], the implicitness can be removed by introducing a transformation,

$$\bar{N}_i(\vec{x},t) = N_i(\vec{x},t) - \frac{\delta_t}{2}[\Omega'_i(\vec{x},t) + F_i(\vec{x},t)]. \tag{A7}$$

Then, the previous implicit scheme Eq. (A6) can be expressed equivalently as

$$\bar{N}_i(\vec{x}+\vec{c}_i\delta_t, t+\delta_t) - \bar{N}_i(\vec{x},t) = \delta_t[\Omega'_i(\vec{x},t) + F_i(\vec{x},t)]. \tag{A8}$$

The collision operator in the D2Q9 MRT model can be given in the form [51,63]

$$\Omega_i' = -(\mathbf{M}^{-1}\mathbf{S}\mathbf{M})_{ij}\left(N_j - N_j^{\mathrm{eq}}\right), \tag{A9}$$

where $\mathbf{M}$ is a transformation matrix and $\mathbf{S} = \mathrm{diag}(\tau_0, \tau_1, \ldots, \tau_8)^{-1}$ is a non-negative diagonal matrix, with τ_i being the relaxation time for the ith moment. Using the transformation matrix, the distribution functions N_i, N_i^{eq}, and $\bar{N}_i$ can be projected onto the moment space as

$$m_i = \mathbf{M}_{ij}N_j, \quad m_i^{\mathrm{eq}} = \mathbf{M}_{ij}N_j^{\mathrm{eq}}, \quad \bar{m}_i = \mathbf{M}_{ij}\bar{N}_j. \tag{A10}$$

Combining Eqs. (A7), (A9), and (A10), the relation between both velocity moments m_i and $\bar{m}_i$ can be expressed as

$$\bar{m}_i = m_i - 0.5\delta_t\left[-\mathbf{S}\left(m_i - m_i^{\mathrm{eq}}\right) + \bar{F}_i\right] \tag{A11}$$

and

$$m_i = (\mathrm{I} + 0.5\delta_t\mathbf{S})^{-1}\left(\bar{m}_i + 0.5\delta_t\mathbf{S}m_i^{\mathrm{eq}} + 0.5\delta_t\bar{F}_i\right), \tag{A12}$$

where $\mathbf{I}$ is the unity matrix and $\bar{F}_i = \mathbf{M}_{ij}F_j$ are the force terms in the moment space.

Utilizing Eqs. (A9)–(A12), the evolution equation (A8) for $\bar{N}_i$ can be easily transformed into the MRT framework and the corresponding collision process can be carried out in the moment space as

$$\bar{m}_i(\vec{x}+\vec{c}_i\delta_t, t+\delta_t) = \bar{m}_i - \delta_t\bar{\mathbf{S}}\left(\bar{m}_i - m_i^{\mathrm{eq}}\right) + \delta_t\mathbf{S}'\bar{F}_i \tag{A13}$$

with

$$\bar{\mathbf{S}} = (\mathbf{S}^{-1} + 0.5\delta_t\mathbf{I})^{-1}, \ \mathbf{S}' = (\mathbf{I} + 0.5\delta_t\mathbf{S})^{-1} = \mathbf{S}^{-1}\bar{\mathbf{S}}. \tag{A14}$$

Substituting Eq. (A4) into Eq. (A7), it can be found that the variables $\bar{N}_i(\vec{x},t)$ and $\bar{N}_i(\vec{x}+\vec{c}_i\delta_t, t+\delta_t)$ actually are the first-order Taylor expansions of $N_i(\vec{x}-\vec{c}_i\delta_t/2, t-\delta_t/2)$ and $N_i(\vec{x}+\vec{c}_i\delta_t/2, t+\delta_t/2)$, respectively, which is the same as the treatment [see Eq. (7)] in the FMLB model.

In addition, note that (i) the external force terms $\bar{F}_i$ can be directly structured in the moment space without computing it from the expression in the disperse velocity space, which is the same as the treatment of the equilibrium moment m_i^{eq} in the standard MRT framework; (ii) in the FMLB model, the external force terms in the moment space can be computed by $\bar{F}_k = \mathbf{E}_{ki}\omega_i\vec{c}_i \cdot \vec{f}/c_s^2 = (0, f_x, f_y, 0, 0, 0, 0, 0, 0)^{\mathrm{T}}$, so Eq. (A1) can be rearranged into the same form as Eq. (A13); (iii) for the conserved moments $\rho\vec{u}$, the corresponding value in the diagonal matrix Λ is fixed at $2/\delta_t$ for the FMLB model, which is equivalent to setting $\tau_{\rho\vec{u}} = 0$ in this MRT framework; that is to say, there are two non-nil relaxation terms in the FMLB model, $(3\nu + \delta_t/2)$ and $\delta_t/(\gamma_1 + 1)$ if collated with this MRT framework, as shown in Eqs. (A13) and (A14).

The comparison discussed above reveals that, with the assumption of $B = 1$, the FMLB model can be completely regarded as a special case (two-relaxation time) of the MRT model with the trapezoidal rule.

APPENDIX B: THE DETAILS OF THE CBBSR SCHEME WITHIN THE FMLB MODEL

For the steady incompressible Poiseuille flow driven by a constant force, as mentioned in Sec. II, the CBBSR scheme within the D2Q9 FMLB model produces the relation between the horizontal velocities near the wall, Eq. (20). In the following, we make a detailed analysis to derive that formula.

First, according to the transformation between the distribution functions N_i and the moments α_i $(i = 0,1,2,\ldots,8)$, we have

$$N_1^{\pm} - N_3^{\pm} = (2\alpha_1^{\pm} - \alpha_6^{\pm})/3, \tag{B1}$$

$$N_5^{\pm} - N_6^{\pm} = (\alpha_1^{\pm} + \alpha_4^{\pm} + \alpha_6^{\pm})/6, \quad N_8^{\pm} - N_7^{\pm} = (\alpha_1^{\pm} - \alpha_4^{\pm} + \alpha_6^{\pm})/6. \tag{B2}$$

Combining the collision expression in the moment space Eq. (A1) and the constraints Eq. (17) while utilizing Eqs. (10)

and (B1), we can obtain

$$\alpha_4^{1,2+} = G\alpha_4^{1,2-}, \tag{B3}$$

$$\alpha_6^{1,2+} = \frac{2\gamma_1}{1+\gamma_1}\rho a\delta_t, \quad \alpha_6^{1,2-} = -\frac{2}{1+\gamma_1}\rho a\delta_t. \tag{B4}$$

Taking the constraint $\partial N_i/\partial x = 0$ into consideration, the transport step between the inner node at $J = 0$, 1, and 2 can be simply written as

$$N_{5,6}^{1-} = N_{5,6}^{0+}, \quad N_{7,8}^{1-} = N_{7,8}^{2+}, \quad N_{5,6}^{2-} = N_{5,6}^{1+}. \tag{B5}$$

Then, substituting Eq. (B5) into Eq. (B2) yields

$$\alpha_1^{1+} + \alpha_4^{1+} + \alpha_6^{1+} = \alpha_1^{2-} + \alpha_4^{2-} + \alpha_6^{2-}, \tag{B6}$$

$$\alpha_1^{1-} - \alpha_4^{1-} + \alpha_6^{1-} = \alpha_1^{2+} - \alpha_4^{2+} + \alpha_6^{2+}. \tag{B7}$$

According to Eq. (10), the momenta $\alpha_1^{1,2\pm}$ are expressed as

$$\alpha_1^{1,2\pm} = \rho u_{1,2} \pm \rho a\delta_t/2. \tag{B8}$$

Combining Eqs. (B3), (B4), and (B6)–(B8), the moment α_4^{1-} can be expressed in the form

$$\alpha_4^{1-} = \frac{\rho\,(u_1 - u_2)}{1-G} - \frac{3\rho a\delta_t}{1+G}. \tag{B9}$$

In addition, from Eqs. (16) and (B5), the CBBSR scheme gives that

$$N_5^{1-} - N_6^{1-} = (1-2r)\left(N_8^{1+} - N_7^{1+}\right). \tag{B10}$$

Then, substituting Eq. (B2) into Eq. (B10) gives

$$\alpha_1^{1-} + \alpha_4^{1-} + \alpha_6^{1-} = (1-2r)\left(\alpha_1^{1+} - \alpha_4^{1+} + \alpha_6^{1+}\right). \tag{B11}$$

With the aid of Eqs. (B3), (B4), (B8), and (B9), we can obtain from Eq. (B11) that

$$u_2 = \left(1 + \frac{2r\,(1-G)}{1+G-2rG}\right)u_1 - \frac{1-G}{1+G-2rG} \times \left[6 - r\left(\frac{6G}{1+G} + \frac{1+5\gamma_1}{1+\gamma_1}\right)\right]\delta_t a. \tag{B12}$$

[1] C. M. Ho and Y. C. Tai, Annu. Rev. Fluid Mech. **30**, 579 (1998).
[2] G. Karniadakis and A. Beskok, *Micro Flows: Fundamentals and Simulation* (Springer, New York, 2002).
[3] W. Zhang, G. Meng, and X. Wei, Microfluid. Nanofluid. **13**, 845 (2012).
[4] S. A. Schaaf and P. L. Chambré, *Flow of Rarefied Gases* (Princeton University Press, Princeton, NJ, 1961).
[5] R. W. Barber and D. R. Emerson, Heat Transf. Eng. **27**, 3 (2006).
[6] G. A. Bird, *Molecular Gas Dynamics and the Direct Simulation of Gas Flows* (Oxford University Press, New York, 1994).
[7] F. Sharipov, J. Micromech. Microeng. **9**, 394 (1999).
[8] K. Xu, Phys. Fluids **15**, 2077 (2003).
[9] K. Xu and Z. Li, J. Fluid Mech. **513**, 87 (2004).
[10] X. Nie, G. D. Doolen, and S. Chen, J. Stat. Phys. **107**, 279 (2002).
[11] C. Lim, C. Shu, X. Niu, and Y. Chew, Phys. Fluids **14**, 2299 (2002).
[12] S. Chen and G. D. Doolen, Annu. Rev. Fluid Mech. **30**, 329 (1998).
[13] S. Succi, *The Lattice Boltzmann Equation for Fluid Dynamics and Beyond* (Clarendon Press, Oxford, 2001).
[14] C. Aidun and J. Clausen, Annu. Rev. Fluid Mech. **42**, 439 (2010).
[15] J. Zhang, Microfluid. Nanofluid. **10**, 1 (2011).
[16] S. Ansumali and I. V. Karlin, Phys. Rev. E **66**, 026311 (2002).
[17] X. Niu, C. Shu, and Y. T. Chew, Europhys. Lett. **67**, 600 (2004).
[18] G. Tang, W. Tao, and Y. He, Phys. Fluids **17**, 058101 (2005).
[19] T. Lee and C. L. Lin, Phys. Rev. E **71**, 046706 (2005).
[20] V. Sofonea and R. F. Sekerka, J. Comput. Phys. **207**, 639 (2005).
[21] Y. Zhang, R. Qin, and D. R. Emerson, Phys. Rev. E **71**, 047702 (2005).
[22] Z. Guo, B. Shi, T.-S. Zhao, and C. Zheng, Phys. Rev. E **76**, 056704 (2007).
[23] Z. Chai, Z. Guo, L. Zheng, and B. Shi, J. Appl. Phys. **104**, 014902 (2008).
[24] F. Verhaeghe, L. S. Luo, and B. Blanpain, J. Comput. Phys. **228**, 147 (2009).
[25] Z. Chai, B. Shi, Z. Guo, and J. Lu, Commun. Comput. Phys. **8**, 1052 (2010).
[26] Z. Guo, C. Zheng, and B. Shi, Phys. Rev. E **77**, 036707 (2008).
[27] T. Reis and P. J. Dellar, Phys. Fluids **24**, 112001 (2012).
[28] X. Shan, X.-F. Yuan, and H. Chen, J. Fluid Mech. **550**, 413 (2006).
[29] S. S. Chikatamarla and I. V. Karlin, Phys. Rev. Lett. **97**, 190601 (2006).
[30] R. Zhang, X. Shan, and H. Chen, Phys. Rev. E **74**, 046703 (2006).
[31] X.-D. Niu, S.-A. Hyodo, T. Munekata, and K. Suga, Phys. Rev. E **76**, 036711 (2007).
[32] S. Ansumali, I. Karlin, S. Arcidiacono, A. Abbas, and N. Prasianakis, Phys. Rev. Lett. **98**, 124502 (2007).
[33] S. H. Kim, H. Pitsch, and I. D. Boyd, J. Comput. Phys. **227**, 8655 (2008).
[34] Y.-H Zhang, X.-J. Gu, R. W. Barber, and D. R. Emerson, Phys. Rev. E **74**, 046704 (2006).
[35] Z. Guo, T. Zhao, and Y. Shi, J. Appl. Phys. **99**, 074903 (2006).
[36] G. Tang, Y. Zhang, X. Gu, and D. Emerson, Europhys. Lett. **83**, 40008 (2008).
[37] Q. Li, Y. He, G. Tang, and W. Tao, Microfluid. Nanofluid. **10**, 607 (2011).
[38] A. Homayoon, A. Isfahani, E. Shirani, and M. Ashrafizadeh, Int. Commun. Heat Mass Transf. **38**, 827 (2011).
[39] A. N. Kalarakis, V. K. Michalis, E. D. Skouras, and V. N. Burganos, Transp. Porous Med. **94**, 385 (2012).
[40] X. Liu and Z. Guo, Comput. Math. Appl. **65**, 186 (2013).
[41] A. Beskok and G. E. Karniadakis, Microscale Thermophys. Eng. **3**, 43 (1999).
[42] G. Karniadakis, A. Beskok, and N. Aluru, *Microflows and Nanoflows: Fundamentals and Simulation* (Springer, New York, 2005).
[43] V. K. Michalis, A. N. Kalarakis, E. D. Skouras, and V. N. Burganos, Microfluid. Nanofluid. **9**, 847 (2010).
[44] C. Zhuo, C. Zhong, and J. Cao, Phys. Rev. E **85**, 046703 (2012).

[45] J. Eggels and J. Somers, Int. J. Heat Fluid Flow **16**, 357 (1995).
[46] C. Zhong, J. Xie, C. Zhuo, S. Xiong, and D. Yin, Chin. Phys. B **18**, 4083 (2009).
[47] C. Zhuo, C. Zhong, and J. Cao, Comput. Math. Appl. **65**, 1863 (2013).
[48] C. Cercignani, *Mathematical Methods in Kinetic Theory* (Plenum, New York, 1990).
[49] S. Yuhong and W. Chan, J. Vac. Sci. Technol. A **22**, 383 (2004).
[50] S. Succi, Phys. Rev. Lett. **89**, 064502 (2002).
[51] Z. Guo and C. Zheng, Int. J. Comput. Fluid Dyn. **22**, 465 (2008).
[52] N. G. Hadjiconstantinou, Phys. Fluids **15**, 2352 (2003).
[53] Y. T. Hsia and G. A. Domoto, J. Lubrication Tech. **105**, 120 (1983).
[54] S. Colin, P. Lalonde, and R. Caen, Heat Transf. Eng. **25**, 23 (2004).
[55] T. Ohwada, Y. Sone, and K. Aoki, Phys. Fluids A **1**, 2042 (1989).
[56] C. Shen, D.-B. Tian, C. Xie, and J. Fan, Microscale Thermophys. Eng. **8**, 423 (2004).
[57] E. B. Arkilic, M. A. Schmidt, and K. S. Breuer, J. Microelectromech. Syst. **6**, 167 (1997).
[58] C. Cercignani, M. Lampis, and S. Lorenzani, Phys. Fluids **16**, 3426 (2004).
[59] J. Maurer, P. Tabeling, P. Joseph, and H. Willaime, Phys. Fluids **15**, 2613 (2003).
[60] S. Colin, Microfluid. Nanofluid. **1**, 268 (2005).
[61] C. Aubert and S. Colin, Microscale Thermophys. Eng. **5**, 41 (2001).
[62] X. He, S. Chen, and G. D. Doolen, J. Comput. Phys. **146**, 282 (1998).
[63] P. Lallemand and L. S. Luo, Phys. Rev. E **61**, 6546 (2000).